





# Testing Evolution of LFQPOs with Mass Accretion Rate in GRS 1915+105 with Insight-HXMT

Honghui Liu<sup>1</sup>, Long Ji<sup>2</sup>, Cosimo Bambi<sup>1</sup> , Pankaj Jain<sup>3</sup>, Ranjeev Misra<sup>4</sup> , Divya Rawat<sup>3</sup>, J. S. Yadav<sup>3</sup>, and Yuexin Zhang<sup>5</sup>

<sup>1</sup> Center for Field Theory and Particle Physics and Department of Physics, Fudan University, 200438 Shanghai, People's Republic of China; [bambi@fudan.edu.cn](mailto:bambi@fudan.edu.cn)

<sup>2</sup> Institut für Astronomie und Astrophysik, Kepler Center for Astro and Particle Physics, Eberhard Karls Universität, Tübingen, Germany

<sup>3</sup> Department of Physics, IIT Kanpur, Kanpur, Uttar Pradesh 208016, India

<sup>4</sup> Inter-University Center for Astronomy and Astrophysics, Ganeshkhind, Pune 411007, India

<sup>5</sup> Kapteyn Astronomical Institute, University of Groningen, PO Box 800, Groningen NL-9700 AV, The Netherlands

Received 2020 December 6; revised 2021 January 14; accepted 2021 January 22; published 2021 March 8

## Abstract

Using the Insight-HXMT observations of GRS 1915+105 when it exhibits low-frequency quasiperiodic oscillations (QPOs), we measure the evolution of the QPO frequency along with disk inner radius and mass accretion rate. We find a tight positive correlation between the QPO frequency and mass accretion rate. Our results extend the finding of previous work with AstroSat to a larger range of accretion rates with independent instruments and observations. Treating the QPO frequency of GRS 1915+105 as the relativistic dynamic frequency of a truncated disk, we are able to confirm the high spin nature of the black hole in GRS 1915+105. We also address the potential of our finding to test general relativity in the future.

*Unified Astronomy Thesaurus concepts:* [High energy astrophysics \(739\)](#); [X-ray astronomy \(1810\)](#); [Compact objects \(288\)](#); [Stellar mass black holes \(1611\)](#)

## 1. Introduction

Quasiperiodic oscillations (QPOs; van der Klis 2005) in the form of narrow peaks in the power spectral density (PSD) are often observed in X-ray binaries (XRBs). The phenomenon is found to have similar characteristics in both neutron star and black hole accreting systems (e.g., Wijnands & van der Klis 1999), suggesting a common physical origin (e.g., accretion/ejection flow).

Over the last three decades, we have accumulated abundant knowledge about the behavior of QPOs in black hole XRBs. Correlation between the QPO frequencies and disk flux in the hard state has been found in some systems (Remillard & McClintock 2006; Motta et al. 2011). There is also clear evidence showing a positive correlation between the lower-frequency break ( $\nu_b$ ) and low-frequency QPOs (LFQPOs; e.g., Wijnands & van der Klis 1999; Belloni et al. 2002). Another tight correlation between LFQPOs and high-frequency QPOs (or broad noise components) is found to exist over a large frequency range (Psaltis et al. 1999). These findings help to put strong constraints on models to explain QPOs.

The LFQPOs have a frequency roughly in the range 0.05–30 Hz. In black hole systems, LFQPOs can be divided into several types (A, B, and C; see Casella et al. 2004, 2005). It has been found in some systems that different types of QPOs occur in different stages of the outburst of black hole transients (Motta et al. 2011). Understanding the origin and mechanism of QPOs can give us important hints on both the accretion/ejection process and the spacetime property near compact objects. For instance, Motta et al. (2014) measured the black hole spin of XTE J1550–564 using a simultaneous detection of type C and high-frequency QPOs. There is also an attempt to estimate black hole mass assuming that the correlation between LFQPOs and the high-energy spectrum index scales with mass (Shaposhnikov & Titarchuk 2007).

Models proposed to explain LFQPOs refer mainly to instabilities or geometric effects. For instance, Tagger & Pellat (1999) proposed a model in which the accretion–ejection

instability of a magnetized accretion disk can connect to QPOs observed in XRBs. Stella & Vietri (1998) interpreted the QPOs in low-mass XRBs (LMXBs) as Lense–Thirring precession of the innermost region of the accretion disk. Also in the frame of Lense–Thirring precession, Ingram et al. (2009) considered the precession of the hot flow inside a truncated disk and were able to explain why the observed maximum frequency is almost constant for all black hole XRBs. These models have been further extended and applied to observation data (Varnière & Tagger 2002; Titarchuk & Fiorito 2004; Cabanac et al. 2010; Ingram & Done 2011; Varnière et al. 2012; Veledina et al. 2013; Karpouzas et al. 2020; Ma et al. 2020). However, we have not reached a unified model that can explain all QPO behaviors.

Recently, Misra et al. (2020) confirmed the high spin of the black hole in GRS 1915+105 using a spectral timing analysis of its X-ray radiation with AstroSat (Yadav et al. 2016; Agrawal 2017) data. The authors were able to simultaneously measure the QPO centroid frequency, disk inner radius, and mass accretion rate. A correlation between the QPO frequency divided by the accretion rate and inner disk radius was found, which is expected if the QPO frequency is related to the dynamic frequency ( $f_{\text{dyn}} = c_s(r)/r$ , where  $c_s$  is the sound speed) of the standard accretion model. This kind of analysis requires both broadband energy coverage (for precision measurement of the disk inner radius) and good timing ability of the instruments. We note that the Chinese X-ray satellite Hard X-ray Modulation Telescope (dubbed Insight-HXMT; Zhang et al. 2014) is also capable of measuring the broadband energy spectrum and fast time variability from XRBs, which offers a good opportunity to trace the coevolution of the QPOs and the disk parameters.

In this paper, we present a spectral timing analysis of GRS 1915+105 observed by Insight-HXMT. The data reduction procedure is summarized in Section 2. We describe the timing and spectral analysis in Section 3. We show the results in Section 4 and discuss the findings in Section 5.

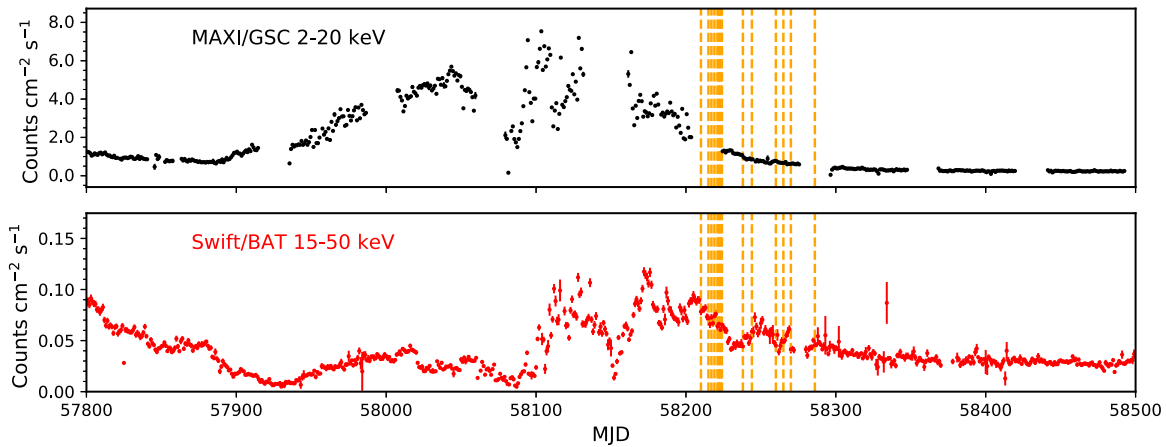


**Figure 1.** MAXI/GSC and Swift/BAT light curves of GRS 1915+105 starting from 2017 February. The vertical orange lines mark Insight-HXMT observations.

## 2. Observation and Data Reduction

Discovered in 1992 by WATCH (Castro-Tirado et al. 1992), GRS 1915+105 is a special LMXB. Unlike other black hole LMXBs that spend most of their time in quiescence, the source has been a persistent system since its discovery. It does not follow the typical Q-shaped pattern on the hardness intensity diagram but instead exhibits a much more complex variability (see Belloni et al. 2000; Hannikainen et al. 2003).

Insight-HXMT extensively observed GRS 1915+105 from 2017 to 2020. We went through all available Insight-HXMT data of GRS 1915+105 and picked out those observations that show QPO signatures. We checked the light curve of each observation and excluded the ones with strong variability (e.g., strong flares or dips). Short exposures on the same day are combined after examining the stability of their light curves. The selected observations analyzed in this work are marked in the light curve of GRS 1915+105 in Figure 1. Information about these observations is listed in Table 1. We also show the hardness ratio and hardness intensity diagram of GRS 1915+105 since 2009 in Figure 2. We use the nearly daily monitoring data of GRS 1915+105 from MAXI and Swift/BAT to create Figure 2. The count rates from both instruments are first scaled into Crab units, and the hardness ratio is defined as the ratio between the scaled MAXI and Swift/BAT count rate.

Insight-HXMT is the first Chinese X-ray telescope and consists of low-, medium-, and high-energy detectors covering the broadband energy range of 1–250 keV (Cao et al. 2020; Chen et al. 2020; Liu et al. 2020; Zhang et al. 2020). We extract light curves and spectra following the official user guide<sup>6</sup> and using the software HXMTDAS ver. 2.02. The background is estimated by the standalone scripts `hebkmap`, `mebkmap`, and `lebkmap` (Guo et al. 2020; Liao et al. 2020a, 2020b). We screen good time intervals by considering the recommended criteria, i.e., an elevation angle  $>10^\circ$ , a geomagnetic cutoff rigidity  $>8$  GeV, a pointing offset angle  $<0.1$ , and at least 300 s away from the South Atlantic Anomaly.

We fit spectral data from the Insight-HXMT Low Energy X-ray Telescope (LE) in the energy range 2–9 keV and the Medium Energy X-ray Telescope (ME) in 8–20 keV. The High Energy X-ray Telescope (HE) data are not included because of

**Table 1**

Insight-HXMT Observations of GRS 1915+105 Analyzed in This Paper

ObsID	Date	Exposure (s)
P0101330005	20180407	1759
P0101330006	20180409	5383
P0101330008	20180411	898
P0101330010	20180413	1399
P0101330011	20180414	3004
P0101330012	20180415	4795
P0101330013	20180416	4489
P0101330016	20180430	3494
P0101330017	20180506	4713
P0101310006	20180527	5043
P0101310007	20180601	6457

**Note.** Only LE exposures are listed. The observation date is presented in the form of `yyyymmdd`.

a strong background presence. We have also checked that adding HE data made little difference to the best-fit parameters.

## 3. Data Analysis

### 3.1. Timing Analysis

We extract the LE light curve of GRS 1915+105 in the 1–10 keV energy band with a time resolution of 1/128 s. Note that we use data in 2–9 keV for spectral analysis (instead of the 1–10 keV for timing analysis) because of the calibration uncertainties of the LE. The nominal time resolution of the LE is 1 ms (corresponding to the Nyquist frequency of 500 Hz), but we are only interested in LFQPOs below 30 Hz in this study and thus a 1/128 s resolution is enough.

We then use the Python package `Stingray` (Huppenkothen et al. 2019) to calculate the PSD with a segment size of 64 s. The final PSD is obtained by averaging all 64 s segments and normalized according to Belloni & Hasinger (1990). We logarithmically rebin the PSD so that each bin size is 1.02 times larger than the previous bin. The PSD is then fitted in XSPEC between 0.1 and 20 Hz using several Lorentzian components

<sup>6</sup> <http://www.hxmt.cn/SoftDoc/67.jhtml>

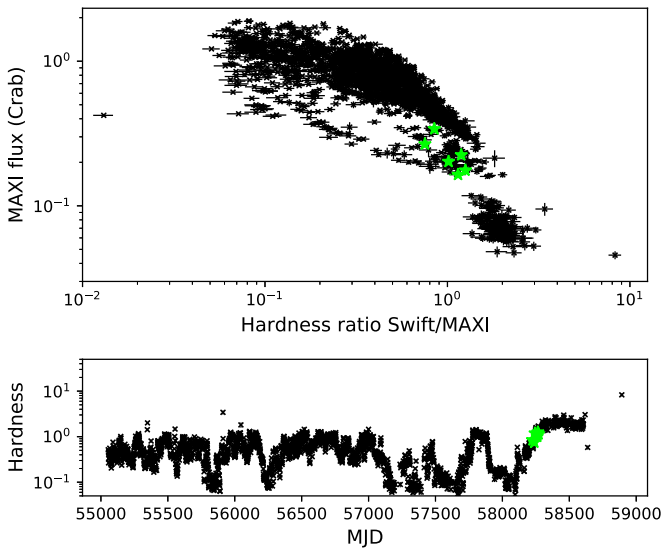


**Figure 2.** Hardness intensity diagram of GRS 1915+105 from MAXI/GSC (2–20 keV) and Swift/BAT (15–50 keV) monitoring. The hardness ratio is defined as the MAXI count rate in Crab units divided by the Swift count rate. The Insight-HXMT observations analyzed in this work are marked with green stars.

(Belloni et al. 2002). We need at least one narrow Lorentzian for the QPO and one zero-centered Lorentzian to fit the broader component. More narrow Lorentzians are sometimes included to model harmonic peaks. All QPOs we detect have a quality factor ( $Q$ ) greater than 4 and detection significance greater than  $3\sigma$ .<sup>7</sup> One typical PSD is shown in Figure 3. The QPO frequencies we find for each observation are listed in Table 2. The ME light curve in the 8–30 keV band has been analyzed in the same way and returns consistent measurements of the QPO frequencies. So we report only the results from LE data in Table 2.

### 3.2. Spectral Analysis

We use XSPEC v12.10.1f (Arnaud 1996) with a cross section set to Verner et al. (1996) to analyze the spectra of GRS 1915+105. As for element abundances, we test both Anders & Grevesse (1989) and Wilms et al. (2000). We find that the choice of abundances does not greatly influence the best-fit parameters (except for  $n_{\text{H}}$ ). This is consistent with what was found by Shreeram & Ingram (2020) in the reflection spectrum of GRS 1915+105. We therefore proceed with further analysis using the abundances of Wilms et al. (2000), which are more up-to-date.

The Insight-HXMT spectra of GRS 1915+105 are fitted with model  $\text{Tbabs} \times (\text{simpl} \times \text{kerrd} + \text{kerrdisk})$ . Model  $\text{Tbabs}$  accounts for absorption by the interstellar medium, and we set its column density ( $n_{\text{H}}$ ) to be free during the fitting. Also included to model the emission from the optically thick accretion disk is  $\text{kerrd}$  (Ebisawa et al. 2003). The black hole mass, distance, and inclination of the accretion disk are set to  $12.4 M_{\odot}$ , 8.6 kpc, and  $60^{\circ}$  (Reid et al. 2014), respectively. We also set the spectral hardening factor of  $\text{kerrd}$  to 1.7 (Shimura & Takahara 1995). Comptonization of disk photons is also taken into account by convolving  $\text{simpl}$  (Steiner et al. 2009) with  $\text{kerrd}$ , and  $\text{kerrdisk}$  (Brenneman & Reynolds 2006) is used to fit possible blurred fluorescent

emission from the accretion disk. The rest-frame line energy is fixed at 6.4 keV (Blum et al. 2009). We fix the spin parameter ( $a_*$ ) to 0.98 and the index of the emissivity profile to 1.8, as done by Misra et al. (2020). Leaving these parameters free will not greatly affect the best-fit values of other parameters. The disk reflection component is always weak (as shown in Figure 3) in the analyzed observations, and the reflection can be well fitted with a simple Gaussian at the iron band. So we do not consider a more sophisticated reflection model (e.g.,  $\text{relxill}$ ; García et al. 2014).

We run a Monte Carlo Markov Chain (MCMC) for each spectrum to estimate the uncertainties of the free parameters. The XSPEC implementation of the MCMC simulation (`Chain` command) using the algorithm of Goodman & Weare (2010) is used to generate the chain. We set up 100 walkers to search the parameter space with the first 5000 steps ignored (burn in). The chain lengths differ from case to case, depending on the autocorrelation of each parameter, but we ensure each walker runs 30 times more steps than the longest autocorrelation length. To further test the convergence of the chain, we compare the two-dimensional distribution for each pair of parameters from the first and second halves of the chain, and we find no large differences.

## 4. Results

The best-fit values and errors extracted from the chains are shown in Table 2. It is interesting to note that although the observations analyzed here are spread over a 2 month interval and the source luminosity decreases by a factor of 3, the QPO signature is always clearly detected. It might be because the corona-disk geometry does not change much during the interval, since the source hardness remains similar for the analyzed observations (see the bottom panel of Figure 2).

Correlation between the QPO frequency, disk inner radius, and accretion rate are shown in Figure 4. We run Spearman’s rank correlation analysis and find that the strongest correlation is between the QPO frequency and mass accretion rate (correlation coefficient  $\rho = 0.89$  with probability of random results  $P < 10^{-3}$ ). The correlation between QPO frequency and disk inner radius is less significant ( $\rho = 0.54$ ,  $P = 8.8\%$ ). Misra et al. (2020) found a stronger correlation between QPO frequency divided by accretion rate and disk inner radius than the correlation between each pair of these parameters. However, the same correlation we find is weaker than that between the QPO frequency and accretion rate, although the correlation is still strong ( $\rho = -0.81$ ,  $P = 0.3\%$ ). We note that the range of mass accretion rate we explored is much larger than that by Misra et al. (2020). This larger range enables us to find the direct dependence of QPO frequency on mass accretion rate.

Misra et al. (2020) identified the QPO frequency of GRS 1915+105 as the dynamic frequency of a truncated disk. The dynamic frequency is defined as the ratio between the sound-crossing velocity at the inner disk and the truncation radius ( $f_{\text{dyn}} \sim c_s(r)/r$ ). Assuming a standard relativistic accretion disk (Novikov & Thorne 1973), the dynamic frequency is a function of black hole spin ( $a_*$ ), mass accretion rate ( $\dot{M}$ ), truncation radius ( $R_{\text{in}}$ ), and overall normalization factor ( $N$ ). Since we can measure the QPO frequency, accretion rate, and truncation radius of GRS 1915+105 with spectral timing analysis, it is

<sup>7</sup> The ratio of the Lorentzian norm divided by its  $1\sigma$  negative error is larger than 3.

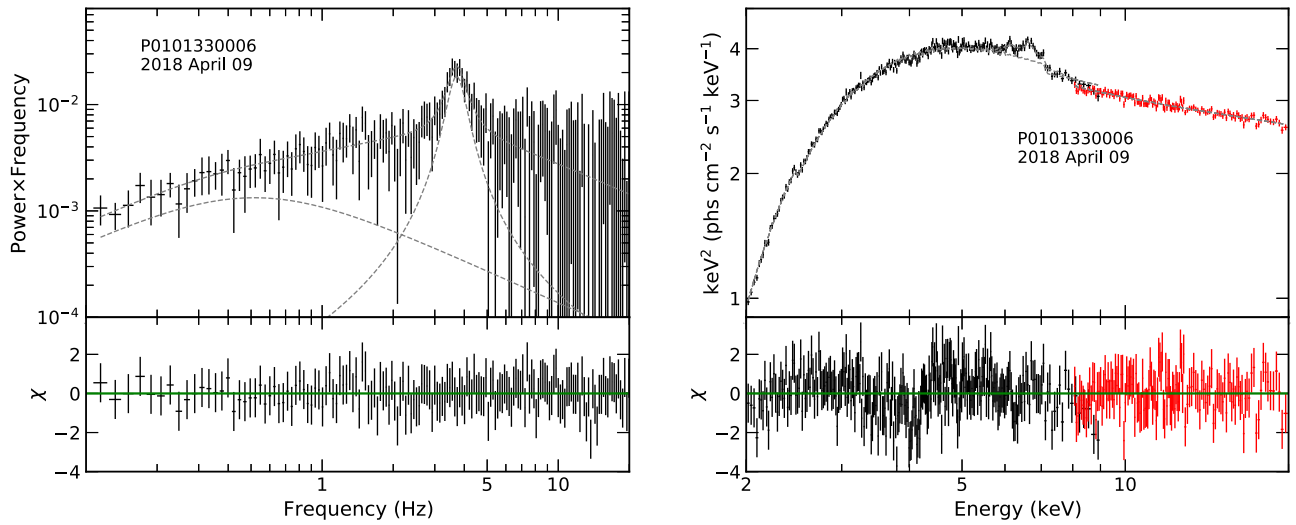


**Figure 3.** Left: PSD of GRS 1915+105 observed by Insight-HXMT on 2018 April 9 in 1–10 keV. Right: Insight-HXMT spectrum of GRS 1915+105 and residuals to the best-fit model. Data from the LE and ME are plotted in black and red, respectively.

**Table 2**  
Best-fit Parameters of GRS 1915+105

Date <sup>1</sup>	$f_a^2$	$f_u^2$	$n_H$ ( $10^{22} \text{ cm}^{-2}$ )	Inner Radius ( $R_g$ )	QPO Frequency (Hz)	Accretion Rate ( $10^{18} \text{ g s}^{-1}$ )	$\Gamma$	Fraction Scatter	$\chi^2/\text{dof}$
20180407	9.8	13.8	$5.66^{+0.21}_{-0.2}$	$4.8^{+0.6}_{-0.5}$	$4.19^{+0.15}_{-0.15}$	$1.32^{+0.15}_{-0.13}$	$2.32^{+0.05}_{-0.05}$	$0.51^{+0.05}_{-0.04}$	436.53/426
20180409	8.4	11.4	$5.27^{+0.12}_{-0.11}$	$4.7^{+0.4}_{-0.3}$	$3.7^{+0.07}_{-0.07}$	$1.05^{+0.08}_{-0.06}$	$2.23^{+0.022}_{-0.022}$	$0.544^{+0.025}_{-0.023}$	845.44/811
20180411	8.5	12.0	$5.61^{+0.24}_{-0.22}$	$4.7^{+0.6}_{-0.5}$	$4.38^{+0.11}_{-0.12}$	$1.2^{+0.15}_{-0.12}$	$2.28^{+0.04}_{-0.04}$	$0.48^{+0.04}_{-0.04}$	341.95/373
20180413	8.3	11.7	$5.6^{+0.2}_{-0.2}$	$4.3^{+0.6}_{-0.5}$	$4.19^{+0.15}_{-0.09}$	$1.08^{+0.12}_{-0.11}$	$2.22^{+0.05}_{-0.06}$	$0.44^{+0.04}_{-0.04}$	329.53/388
20180414	7.5	10.6	$5.56^{+0.16}_{-0.16}$	$4.5^{+0.5}_{-0.4}$	$4.02^{+0.15}_{-0.15}$	$1.0^{+0.09}_{-0.08}$	$2.26^{+0.03}_{-0.04}$	$0.48^{+0.03}_{-0.03}$	608.07/635
20180415	7.9	11.0	$5.78^{+0.25}_{-0.24}$	$4.5^{+0.7}_{-0.6}$	$4.25^{+0.14}_{-0.14}$	$1.06^{+0.15}_{-0.12}$	$2.22^{+0.06}_{-0.06}$	$0.43^{+0.05}_{-0.04}$	301.74/331
20180416	6.7	9.1	$5.1^{+0.19}_{-0.17}$	$4.8^{+0.7}_{-0.6}$	$3.35^{+0.06}_{-0.06}$	$0.79^{+0.1}_{-0.08}$	$2.15^{+0.021}_{-0.022}$	$0.603^{+0.029}_{-0.027}$	833.9/743
20180430	5.2	7.1	$5.06^{+0.17}_{-0.16}$	$3.7^{+0.4}_{-0.4}$	$3.93^{+0.19}_{-0.22}$	$0.57^{+0.06}_{-0.05}$	$2.175^{+0.027}_{-0.027}$	$0.469^{+0.024}_{-0.023}$	589.93/616
20180506	4.7	6.1	$4.35^{+0.18}_{-0.18}$	$2.5^{+0.5}_{-0.9}$	$3.35^{+0.09}_{-0.08}$	$0.34^{+0.04}_{-0.04}$	$2.08^{+0.026}_{-0.023}$	$0.557^{+0.027}_{-0.023}$	708.31/652
20180527	3.5	4.5	$4.3^{+0.17}_{-0.1}$	$1.8^{+0.8}_{-P}$	$3.06^{+0.06}_{-0.05}$	$0.208^{+0.03}_{-0.008}$	$2.064^{+0.02}_{-0.019}$	$0.655^{+0.029}_{-0.027}$	519.54/556
20180601	3.3	4.2	$4.09^{+0.12}_{-0.1}$	$1.7^{+0.7}_{-P}$	$2.62^{+0.07}_{-0.07}$	$0.172^{+0.017}_{-0.006}$	$2.05^{+0.016}_{-0.016}$	$0.79^{+0.03}_{-0.03}$	669.21/621

**Note.** (a) The observation date is presented in the form of  $yyymmdd$ . (b) The absorbed and unabsorbed flux in the 2–10 keV energy band in units  $10^{-9} \text{ erg s}^{-1} \text{ cm}^{-2}$ . Uncertainties correspond to the 5th and 95th percentiles from the MCMC samples. The symbol  $P$  means that the error bar touches the lower (or higher) limit.

possible to infer the spin parameter by fitting the correlation of these parameters (using Equation (3) of Misra et al. 2020).

We fit the relation between QPO frequency divided by accretion rate and disk inner radius using Equation (3) of Misra et al. (2020). The fit on Insight-HXMT data returns  $a_* = 0.99897 \pm 0.00019$  and  $N = 0.108 \pm 0.006$ . We also try to fit the Insight-HXMT and AstroSat data simultaneously, and we get  $a_* = 0.99836 \pm 0.00028$  and  $N = 0.121 \pm 0.005$ , indicating a rapidly spinning black hole in GRS 1915+105. This measurement of high spin is consistent with what has been obtained by analyzing the blurred reflection spectra (Blum et al. 2009; Miller et al. 2013; Zhang et al. 2019b) or thermal spectra (McClintock et al. 2006) of GRS 1915+105. The best-fit curve

is shown in Figure 5, as well as the results of Misra et al. (2020).

From Table 2, we see that the column density of  $T_{\text{babs}}$  evolves with the inner radius and mass accretion rate, which raises the question whether the degeneracy of these parameters affects the measurements. In Figure 6, we plot the degeneracy of the three parameters for two observations (one has the highest absorption column and the other has the lowest). There is indeed a strong correlation between the inner radius and mass accretion rate, which is expected, since a smaller inner radius can somehow compensate for the effect on the spectral shape by a lower accretion rate. This can also explain the degeneracy between the column density of the absorption material and the accretion rate. However, we find that

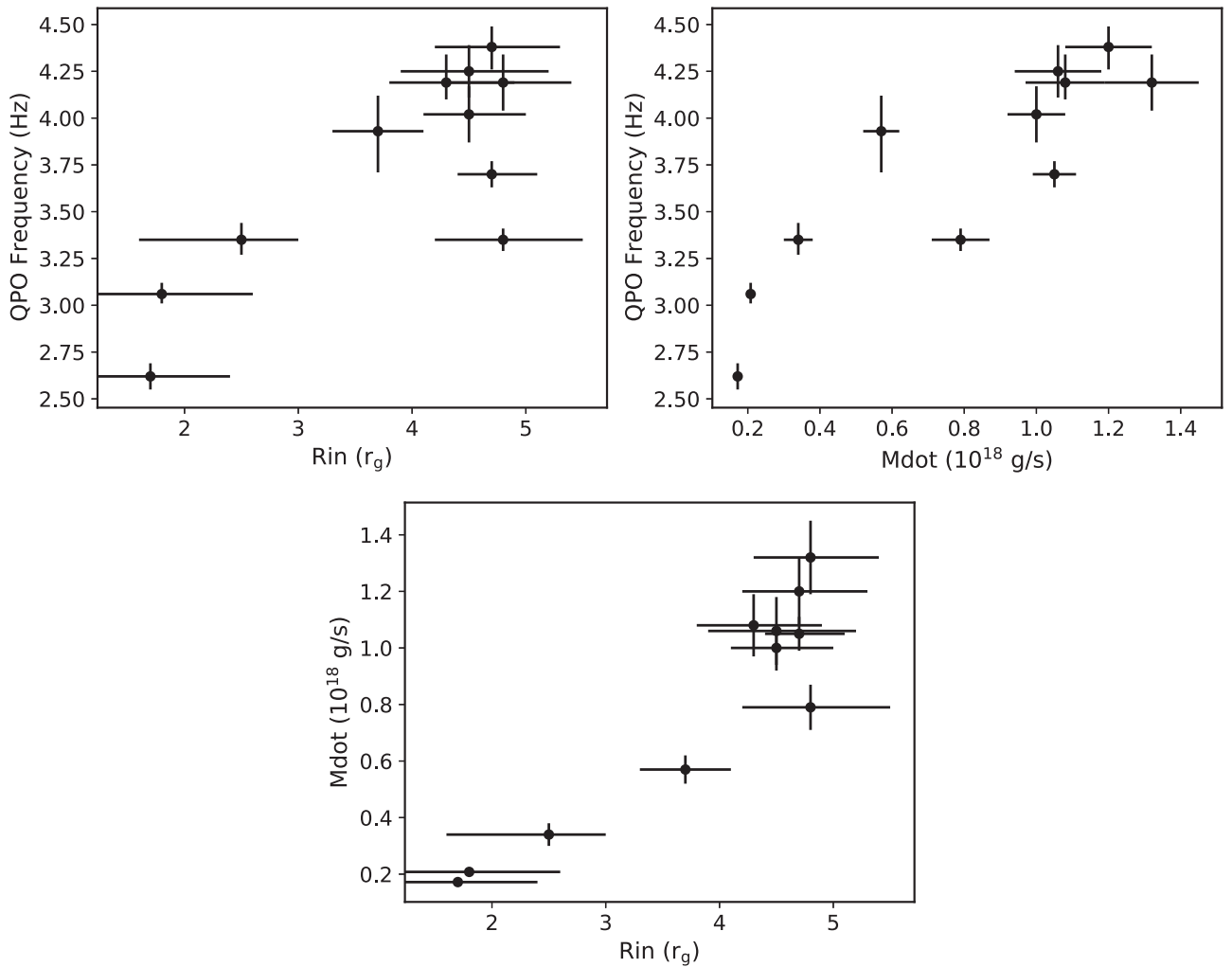


**Figure 4.** The QPO frequency vs. disk inner radius (upper left), QPO frequency vs. accretion rate (upper right), and accretion rate vs. disk inner radius (lower).

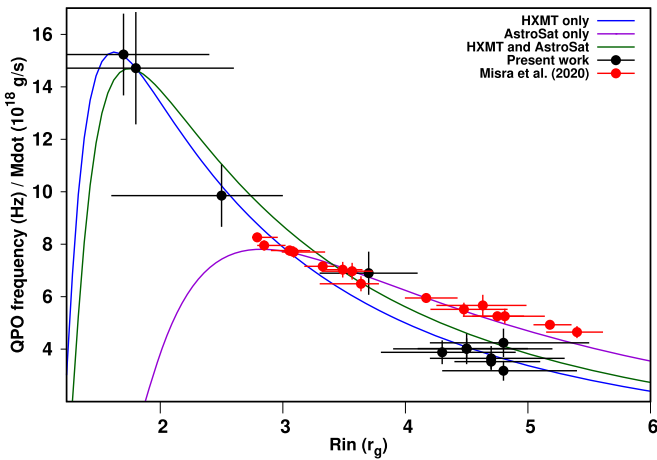


**Figure 5.** The QPO frequency divided by accretion rate with disk inner radius. The black and red crosses denote the results of this work and Misra et al. (2020), respectively. The blue curve represents the best fit of Insight-HXMT data only (reduced  $\chi^2 = 0.22$ ), and the green curve shows the fitting for both Insight-HXMT and AstroSat data (reduced  $\chi^2 = 0.76$ ).

these parameters are well constrained, and we conclude that letting  $n_H$  free will not include bias on the measurement. We have also checked that holding the column density to be the same for all observations provides unacceptable fits.

## 5. Discussion and Conclusions

With the advantage of the broad energy coverage and good time resolution of Insight-HXMT, we measure the evolution of the LFQPO signature of GRS 1915+105 along with its mass accretion rate and inner disk radius. Assuming the QPO frequency corresponds to the relativistic dynamic frequency of the disk, we are able to confirm the high spin nature of the black hole in GRS 1915+105. Our results extend the previous finding with AstroSat (Misra et al. 2020).

In Figure 5, the best-fit curve of Misra et al. (2020) differs substantially from ours for low values of  $R_{in}$ . This is due to the lack of data with low values of the disk inner radius in their analysis. At larger values of  $R_{in}$  ( $R_{in} > 4r_g$  in Figure 5), our data are systematically lower than the AstroSat result. This is why the joint fit (green line) does not agree well with the data. We note that the dynamic frequency model is a very simple assumption. It might not be able to capture all of the factors that drive the variability of the LFQPOs of this source. So it is not a surprise that we find some differences between different observations.

It is instructive to see that such a simple model can already roughly explain the behavior of LFQPOs in GRS 1915+105. However, we note that there are still substantial locations in the hardness intensity diagram of the source not explored in this study (see Figure 2). Thus, more observations of GRS 1915

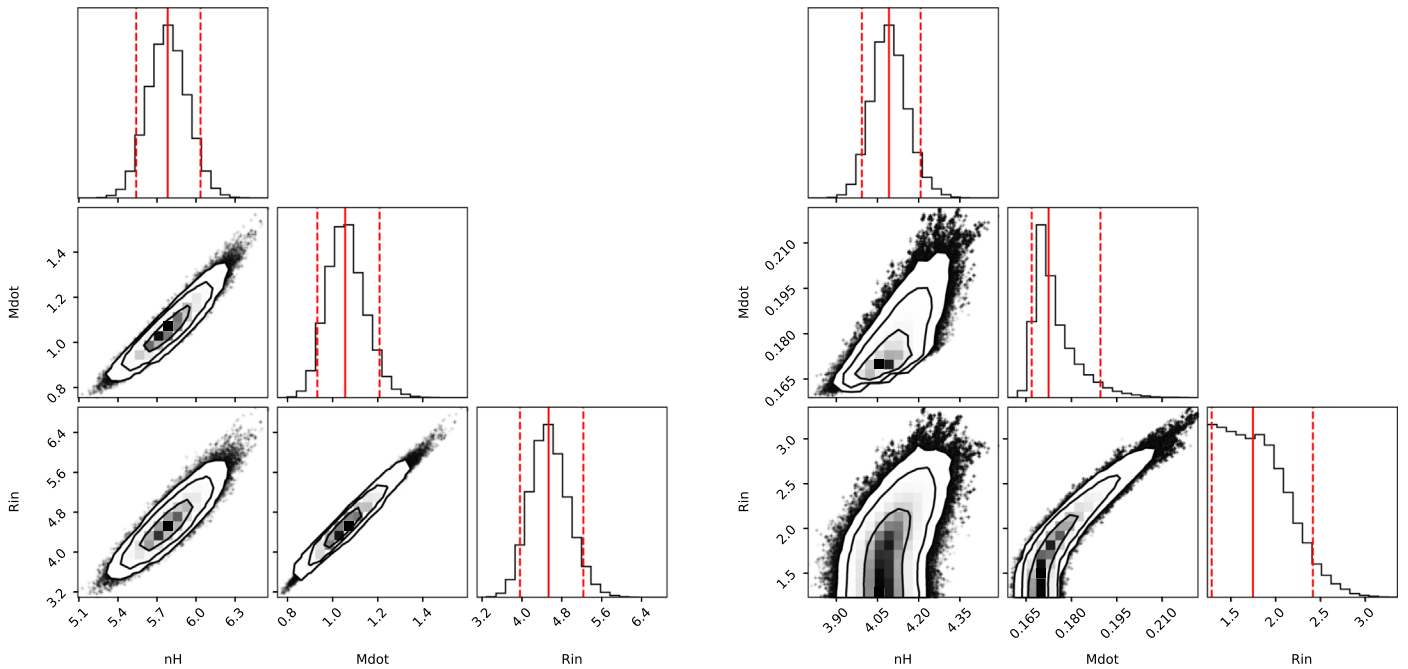


**Figure 6.** Correlation between the column density, disk inner radius, and mass accretion rate for observations on 20180415 (left) and 20180601 (right). The red vertical lines denote the 5th, 50th, and 95th percentiles for individual parameters.

+105 by Insight-HXMT (and AstroSat) are certainly needed to understand the variability of this source.

We note that, although the dynamic frequencies of a truncated disk can fit the behavior of LFQPOs in GRS 1915+105, an explanation of how the oscillation is generated is still missing. The Lense–Thirring precession model would predict a direct dependence of QPO frequency on the disk inner radius (see Ingram et al. 2009; Ingram & Done 2010). However, we find a stronger dependence on mass accretion rate. The precession model also predicts an anticorrelation between LFQPOs and the disk inner radius, which is opposite to what we find (see upper left panel of Figure 4). These discrepancy may suggest that, in this particular case, the precession model is not favored. Note that in the “transition layer model” proposed by Titarchuk & Fiorito (2004), the mass accretion rate can indeed influence LFQPO frequencies by affecting the  $\gamma$ -parameter (Reynolds number) of the accretion disk. The relation they derived between QPO frequency and  $\gamma$ -parameter (which is proportional to mass accretion rate) is very similar in shape to what we find (see Figure 3 of Titarchuk & Fiorito 2004 and upper right panel of Figure 4). This model might be promising to explain the origin of the LFQPOs we find in GRS 1915+105, but further and more detailed investigation is certainly needed.

The lower panel of Figure 4 shows that the inner disk radius tends to decrease when the accretion rate is decreasing (also when the source flux is decreasing). This is counterintuitive, as we will expect the opposite for a truncated disk (Done et al. 2007). For typical X-ray transients (e.g., GX 339-4), the disk is believed to be truncated at large radii at the beginning of the outburst, and the inner edge moves to smaller radii as the mass accretion rate increases (see Esin et al. 1997). There is evidence from observations that supports this scenario (e.g., Wang-Ji et al. 2018; Chainakun et al. 2021). However, GRS 1915+105 is a source with particular properties (see Belloni et al. 2000). It is a persistent source that spends decades accreting at a near-

Eddington rate. The accretion dynamics is more complicated if the disk is thick. For instance, in the case of the Polish doughnut model (Abramowicz et al. 1978), the inner edge of the disk is determined by the fluid angular momentum. If the fluid angular momentum increases as the mass accretion rate increases, the inner edge will move to larger radii. Moreover, when calculating the evaporation of ion-irradiated disks, Dullemond & Spruit (2005) also found that the inner radius of the cold disk increases with increasing mass accretion rate, which is due to the larger circumference needed to transfer all of the matter. These scenarios may explain what we are seeing on GRS 1915+105.

We would also like to address the potential of our finding on testing general relativity in the strong field regime (e.g., Bambi 2017). Once the origin of the QPOs is understood, the behavior of the QPOs can help to reveal the spacetime properties in the vicinity of the black hole (e.g., Motta et al. 2014). We have been able to test the Kerr hypothesis using the reflection-dominated (Zhang et al. 2019b) and thermal-dominated (Tripathi et al. 2020) X-ray spectra of black hole XRBs, although systematic uncertainties in modeling can somehow affect the analysis (e.g., Liu et al. 2019; Zhang et al. 2019a; Riaz et al. 2020). In the particularly interesting source GRS 1915+105, we can apply the continuum fitting method, reflection spectroscopy, and QPO modeling together to constrain a possible deviation from the Kerr metric. We would expect a tight constraint from the combination of these techniques. This will be further explored in future work.

The work of H.L. and C.B. is supported by the Innovation Program of the Shanghai Municipal Education Commission, grant No. 2019-01-07-00-07-E00035; the National Natural Science Foundation of China (NSFC), grant No. 11973019; and Fudan University, grant No. JIH1512604. J.L. is thankful for the support of the National Natural Science Foundation of China under grant Nos. 11733009, U1938103, and U2038101.

## ORCID iDs

Cosimo Bambi  <https://orcid.org/0000-0002-3180-9502>  
 Ranjeev Misra  <https://orcid.org/0000-0002-7609-2779>

## References

- Abramowicz, M., Jaroszynski, M., & Sikora, M. 1978, *A&A*, **63**, 221  
 Agrawal, P. C. 2017, *JApA*, **38**, 27  
 Anders, E., & Grevesse, N. 1989, *GeCoA*, **53**, 197  
 Arnaud, K. A. 1996, in ASP Conf. Ser. 101, *Astronomical Data Analysis Software and Systems V*, ed. G. H. Jacoby & J. Barnes (San Francisco, CA: ASP), 17  
 Bambi, C. 2017, *RvMP*, **89**, 025001  
 Belloni, T., & Hasinger, G. 1990, *A&A*, **227**, L33  
 Belloni, T., Klein-Wolt, M., Méndez, M., van der Klis, M., & van Paradijs, J. 2000, *A&A*, **355**, 271  
 Belloni, T., Psaltis, D., & van der Klis, M. 2002, *ApJ*, **572**, 392  
 Blum, J. L., Miller, J. M., Fabian, A. C., et al. 2009, *ApJ*, **706**, 60  
 Brenneman, L. W., & Reynolds, C. S. 2006, *ApJ*, **652**, 1028  
 Cabanac, C., Henri, G., Petrucci, P. O., et al. 2010, *MNRAS*, **404**, 738  
 Cao, X., Jiang, W., Meng, B., et al. 2020, *SCPMA*, **63**, 249504  
 Casella, P., Belloni, T., Homan, J., & Stella, L. 2004, *A&A*, **426**, 587  
 Casella, P., Belloni, T., & Stella, L. 2005, *ApJ*, **629**, 403  
 Castro-Tirado, A. J., Brandt, S., & Lund, N. 1992, *IAUC*, **5590**, 2  
 Chainakun, P., Luangtip, W., Young, A. J., Thongkongsing, P., & Srichok, M. 2021, *A&A*, **645**, A99  
 Chen, Y., Cui, W., Li, W., et al. 2020, *SCPMA*, **63**, 249505  
 Done, C., Gierliński, M., & Kubota, A. 2007, *A&ARv*, **15**, 1  
 Dullemond, C. P., & Spruit, H. C. 2005, *A&A*, **434**, 415  
 Ebisawa, K., Życki, P., Kubota, A., Mizuno, T., & Watarai, K.-y. 2003, *ApJ*, **597**, 780  
 Esin, A. A., McClintock, J. E., & Narayan, R. 1997, *ApJ*, **489**, 865  
 García, J., Dauser, T., Lohfink, A., et al. 2014, *ApJ*, **782**, 76  
 Goodman, J., & Weare, J. 2010, *CAMCS*, **5**, 65  
 Guo, C.-C., Liao, J.-Y., Zhang, S., et al. 2020, *JHEAp*, **27**, 44  
 Hannikainen, D. C., Vilhu, O., Rodríguez, J., et al. 2003, *A&A*, **411**, L415  
 Huppenkothen, D., Bachetti, M., Stevens, A. L., et al. 2019, *ApJ*, **881**, 39  
 Ingram, A., & Done, C. 2010, *MNRAS*, **405**, 2447  
 Ingram, A., & Done, C. 2011, *MNRAS*, **415**, 2323  
 Ingram, A., Done, C., & Fragile, P. C. 2009, *MNRAS*, **397**, L101  
 Karpouzas, K., Méndez, M., Ribeiro, E. R. M., et al. 2020, *MNRAS*, **492**, 1399  
 Liao, J.-Y., Zhang, S., Chen, Y., et al. 2020a, *JHEAp*, **27**, 24  
 Liao, J.-Y., Zhang, S., Lu, X.-F., et al. 2020b, *JHEAp*, **27**, 14  
 Liu, C., Zhang, Y., Li, X., et al. 2020, *SCPMA*, **63**, 249503  
 Liu, H., Abdikamalov, A. B., Ayzenberg, D., et al. 2019, *PhRvD*, **99**, 123007  
 Ma, X., Tao, L., Zhang, S.-N., et al. 2020, *NatAs*, **5**, 94  
 McClintock, J. E., Shafee, R., Narayan, R., et al. 2006, *ApJ*, **652**, 518  
 Miller, J. M., Parker, M. L., Fuerst, F., et al. 2013, *ApJL*, **775**, L45  
 Misra, R., Rawat, D., Yadav, J. S., & Jain, P. 2020, *ApJL*, **889**, L36  
 Motta, S., Muñoz-Darias, T., Casella, P., Belloni, T., & Homan, J. 2011, *MNRAS*, **418**, 2292  
 Motta, S. E., Muñoz-Darias, T., Sanna, A., et al. 2014, *MNRAS*, **439**, L65  
 Novikov, I. D., & Thorne, K. S. 1973, in *Black Holes (Les Astres Occlus)*, ed. C. DeWitt & B. DeWitt (New York: Gordon and Breach), 343  
 Psaltis, D., Belloni, T., & van der Klis, M. 1999, *ApJ*, **520**, 262  
 Reid, M. J., McClintock, J. E., Steiner, J. F., et al. 2014, *ApJ*, **796**, 2  
 Remillard, R. A., & McClintock, J. E. 2006, *ARA&A*, **44**, 49  
 Riaz, S., Ayzenberg, D., Bambi, C., & Nampalliwar, S. 2020, *MNRAS*, **491**, 417  
 Shaposhnikov, N., & Titarchuk, L. 2007, *ApJ*, **663**, 445  
 Shimura, T., & Takahara, F. 1995, *ApJ*, **445**, 780  
 Shreeram, S., & Ingram, A. 2020, *MNRAS*, **492**, 405  
 Steiner, J. F., Narayan, R., McClintock, J. E., & Ebisawa, K. 2009, *PASP*, **121**, 1279  
 Stella, L., & Vietri, M. 1998, *ApJL*, **492**, L59  
 Tagger, M., & Pellat, R. 1999, *A&A*, **349**, 1003  
 Titarchuk, L., & Fiorito, R. 2004, *ApJ*, **612**, 988  
 Tripathi, A., Zhou, M., Abdikamalov, A. B., et al. 2020, *ApJ*, **897**, 84  
 van der Klis, M. 2005, *AN*, **326**, 798  
 Varnière, P., & Tagger, M. 2002, *A&A*, **394**, 329  
 Varnière, P., Tagger, M., & Rodríguez, J. 2012, *A&A*, **545**, A40  
 Veledina, A., Poutanen, J., & Ingram, A. 2013, *ApJ*, **778**, 165  
 Verner, D. A., Ferland, G. J., Korista, K. T., & Yakovlev, D. G. 1996, *ApJ*, **465**, 487  
 Wang-Ji, J., García, J. A., Steiner, J. F., et al. 2018, *ApJ*, **855**, 61  
 Wijnands, R., & van der Klis, M. 1999, *ApJ*, **514**, 939  
 Wilms, J., Allen, A., & McCray, R. 2000, *ApJ*, **542**, 914  
 Yadav, J. S., Agrawal, P. C., Antia, H. M., et al. 2016, *Proc. SPIE*, **9905**, 99051D  
 Zhang, S., Lu, F. J., Zhang, S. N., & Li, T. P. 2014, *Proc. SPIE*, **9144**, 91442I  
 Zhang, S.-N., Li, T., Lu, F., et al. 2020, *SCPMA*, **63**, 249502  
 Zhang, Y., Abdikamalov, A. B., Ayzenberg, D., et al. 2019a, *ApJ*, **875**, 41  
 Zhang, Y., Abdikamalov, A. B., Ayzenberg, D., Bambi, C., & Nampalliwar, S. 2019b, *ApJ*, **884**, 147